Energy Conversion and Management 88 (2014) 177–188

Contents lists available at ScienceDirect

Energy Conversion and Management

journal homepage: www.elsevier.com/locate/enconman

A computational fluid dynamics study on the heat transfer characteristics of the working cycle of a β-type Stirling engine

Jose Leon Salazar [a], Wen-Lih Chen [b,*]

[a] Material Engineering School, Costa Rica Institute of Technology, Cartago, Costa Rica
[b] Clean Energy Center, Department of Mechanical Engineering, Kun Shan University Yung-Kang, Tainan 710-03, Taiwan, ROC

ARTICLE INFO

Article history:
Received 30 May 2014
Accepted 16 August 2014

Keywords:
β-Type Stirling engine
CFD
Compressible flow

ABSTRACT

A compressible CFD code has been developed to study the heat transfer characteristics of a β-type Stirling engine with a very simple design and geometry. The results include temperature contours, velocity vectors, and distributions of local heat flux along solid boundaries at several important time steps as well as variations of average temperatures, integrated rates of heat input, heat output, and engine power. It is found that impingement is the major heat transfer mechanism in the expansion and compression chamber, and the temperature distribution is highly non-uniform across the engine at any given moment. The results, especially the rates of heat transfer, are quite different from those obtained by a second-order model. The variations of heat transfer rates are much more complicated than the simple variations returned by the second-order model. This study sheds light into the complex heat transfer mechanism inside the Stirling engine and is very helpful to the understanding of the fundamental process of the engine cycle.

© 2014 Elsevier Ltd. All rights reserved.

1. Introduction

Stirling engine, a nearly 200 years old invention, has attracted much attention and been the subject of intensive research by many industrial and academic institutes alike in recent decades due to its many specific advantages [1–4]. These advantages are: very high efficiency, silence in operation, low level of toxic emission if powered by fuel, and the ability to use almost any kind of heat sources, including solar, biological, geothermal, or even industrial waste heat. Nowadays, it has been regarded as an important green energy device and potentially one of the most promising solutions to the global warming problem. Among its most successful applications is the micro combined heat and power (CHP) systems where the power output of the engine is used to generate electricity, and the waste heat from engine cycle is used for heating purpose [5–7]. However, there are also disadvantages associated with Stirling engines. It is low in the power/weight ratio, unable to change torque and power swiftly, and expensive (especially for those using concentration solar energy); and these have precluded the engine's spread to more general applications. Despite these disadvantages, Stirling engine technology has been constantly improved to produce new generation of engines with higher power/weight ratio, efficiency, and power output; and Stirling engines might become more popular and spread to more general applications in the future.

Improvement on Stirling engine's performance relies heavily on extensive numerical and experimental research. To design a new Stirling engine, a numerical analysis often precedes experiment to find some general directions to follow. It is also a more suitable tool than experiment to carry out parameter optimization. Therefore, many numerical models for Stirling engine cycle have been developed. A detailed overview of the existing numerical models for Stirling engine cycles can be found in Mahkamov [8]. These models are broadly classified as the first-, second-, and third-order models, according to the model hierarchy. Here, the term "order" has nothing to do with the mathematical terms in the governing equations. In these models, the entire engine is divided into 3, or 5, or more sections (control volumes), so they are practically zero- or one-dimensional models. Among them, the model proposed by Schmidt is the stereotype, and improved variants of Schmidt's model are nowadays the most widely adopted Stirling engine models [9–11]. However, because these models are zero- or one-dimensional models, they, at best, only resolve spatial variations in the axial direction of the engine. In this case, any variation in the transverse direction that is important for predicting the engine's performance accurately will not be accounted for. Neither can they resolve the effects caused by changes in some geometrical

* Corresponding author.
E-mail address: wlchen@mail.ksu.edu.tw (W.-L. Chen).

http://dx.doi.org/10.1016/j.enconman.2014.08.040
0196-8904/© 2014 Elsevier Ltd. All rights reserved.

Nomenclature

c_p	constant pressure specific heat (kJ kg^{-1} K^{-1})
G	regenerative channel gap (m)
h	heat transfer coefficient (W K^{-1})
k	thermal conductivity (W m^{-1} K^{-1})
l_d	height of displacer (m)
L_t	height of the engine (m)
l_1, l_2, l_3, l_4	lengths of the linkages of the rhombic drive mechanism (m)
L	distance between two gears (m)
L_{dt}	length from the linkage l_4 to top surface of the displacer (m)
L_{pt}	height from the linkage l_1 to top surface of the piston (m)
m	mass of working gas (kg)
p	pressure (Pa or N m^{-2})
q	heat flux or heat transfer rate per unit area (W m^{-2})
Q_{in}	input heat transfer rate (W)
Q_{out}	output heat transfer rate (W)
r, x	two-dimensional cylindrical coordinates
r_1	radius of the displacer (m)
r_2	core radius of cylinder (m)
$\bar{R}$	gas constant (J kg^{-1} K^{-1})
R_d	offset distance from the crank to the center of gear (m)
t	time (s)
t_p	time period of an engine cycle
T	temperature (K)
u, v	velocity components respectively in x- and r-directions (ms^{-1})
$\tilde{u}$, $\tilde{v}$	local frame moving velocity components respectively in x- and r-directions (ms^{-1})
$\bar{v}$	specific volume of working gas (m^3 kg^{-1})
V	volume (m^3)
W	engine power (W)

Greeks

ρ	density (kg m^{-3})
δ	wall thickness of the core cylinder (m)
η	engine efficiency
θ	crank angle
ω	engine speed (rad s^{-1})

Subscripts

f	fluid
s	solid

features such as the geometries and dimensions of displacer and displacer cylinder, regeneration chamber, or the internal gas circuits, all of which can only be defined in multi dimensions. This means that they are not very useful in terms of the optimization of the geometries and dimensions of individual components during the design of a Stirling engine. In addition, heat transfer rates inside the expansion and compression chambers are often estimated by using constant convective heat transfer coefficients, a practice that has over-simplified the complexity of the real heat transfer mechanism taking place inside these chambers. These factors together with other model assumptions result in poor predictive accuracy returned by these models. They tend to over-predict engine's output power and efficiency by the margins from 30% to 100%, or even more [8].

A Stirling cycle involves very complicated heat and mass transfer processes, and the engine itself consists of many multi-dimensional components whose geometrical effects can be important. None of these can be resolved in great detail or very accurately by those aforementioned numerical models. Yet, resolving these complicated physical processes and the effects from some geometrical features is crucial to the prediction of the overall engine performance. Especially understanding the effects of the geometrical features is of practical importance because to design a new Stirling engine, engineers have to determine the detail geometries and dimensions of all components in the engine. Therefore, more sophisticated models are needed to improve the accuracy of the numerical analysis on Stirling engines. Computational fluid dynamics (CFD) is one of such numerical approaches by far that are capable of simulating those complicated processes taking place in Stirling engine and hence returning accurate prediction on the overall engine performance. It is also capable of resolving the effects caused by changes in small geometrical features and potentially be a great tool for the design and development of a new Stirling engine. However, there exist many challenges to apply a CFD analysis on a Stirling engine cycle. A Stirling engine cycle is unsteady and multi-scale in nature. In addition, the engine involves moving parts such as displacer and power piston; hence the volume of computational domain is constantly changing with time. These bring challenges in coding and physical modeling. In the aspect of coding, simulating the reciprocating motions of displacer and power piston requires the use of moving mesh techniques which involve complex algorithms. In the aspect of physical modeling, the gas flow is compressible; the heat transfer mechanism is conjugate heat transfer; and in most cases, the flow is turbulent. The combination of these factors gives rise to very complicated heat and mass transfer processes. To resolve these processes, it is necessary to use very fine grids and small time steps and solve many coupled governing equations at the same time, resulting in difficulty of convergence and long CPU time. Due to these challenges, many attempts to apply CFD analysis on Stirling engines focused on individual components such as the combustion chamber of the heater [12]. So far, there have been few reports on using CFD approach to study the full cycle of a Stirling engine. Mahkamov [8] used both second-order approach and axisymmetric CFD approach to analyze the working process of a solar Stirling engine. They found significant differences in temperature data and engine performance obtained by both methods. The transient temperature variations by CFD approach were far from the harmonic distributions given by the second-order approach, and CFD model returned much accurate output power than the second-order model. Mahkamov [13] also reported applying a 3D CFD approach on a prototype biomass Stirling engine to improve its performance. The engine was also analyzed by the first-order and second-order models. The CFD analysis identified some key factors that reduce the power of the engine: a geometrical feature that causes high level of hydraulic losses in the regenerator, and the entrapment of the gas in the pipe connecting two parts of the compression space and the dead volume introduced by the pipe. Such detailed analysis on the effects imposed by multi-dimensional geometrical features can only be resolved by using a CFD approach. The research also highlighted the usefulness of adopting a CFD approach to identify and solve problems during the design of a Stirling engine. Zhigang et al. [14] used CFD approach to investigate the effect of a regenerator filled with porous-sheets heat exchangers. The CFD results were found in very good agreement with experimental data, further proving the capability of the CFD

approach to return accurate prediction on Stirling engine performance. Chen et al. [15] conducted a CFD study on the heat transfer characteristics of the working cycle of a 3D γ-type Stirling engine. It was found that impingement is the major heat transfer mechanism in the expansion and compression chambers, and the temperature distribution is three dimensional and highly non-uniform across the engine volume at any given moment.

Although CFD approach has been applied to the research and development of industrial Stirling engines, in open literature, there has not been a detailed CFD study on the basic heat transfer processes in the Stirling engine cycle. Yet, understanding the fundamental processes of the Stirling engine cycle in great detail is a key step to improve the engine's performance. The objective of this study is to perform CFD analysis on the working cycle of a β-type Stirling engine to reveal the characteristics of its heat transfer processes. This particular type of Stirling engine cycle was chosen because of its large cycle power, high thermal efficiency, and popularity. It has been widely studied before by zero- or one-dimensional models, therefore comparison can be made between the results obtained in this study and those in literature.

2. Mathematical model

The Stirling engine analyzed in this study is the rhombic-drive β-type Stirling engine developed by Cheng and Yu [16], where the engine was analyzed by an improved variant of the second-order model. The schematic of the geometrical configuration of the engine is given in Fig. 1. According to Fig. 1, the displacements of the piston and displacer are:

$$X_p(t) = L_{pt} + R_d \sin\theta + \left[l_2^2 - \left(\frac{L}{2} - \frac{l_1}{2} - R_d\cos\theta\right)^2\right]^{0.5}, \quad (1)$$

$$X_d(t) = L_{dt} + R_d \sin\theta - \left[l_3^2 - \left(\frac{L}{2} - \frac{l_4}{2} - R_d\cos\theta\right)^2\right]^{0.5}, \quad (2)$$

and the velocities of piston and displacer are:

$$u_p(t) = R_d\omega\left\{\cos\theta - \sin\theta\left[l_2^2 - \left(\frac{L}{2} - \frac{l_1}{2} - R_d\cos\theta\right)^2\right]^{-0.5} \times\left(\frac{L}{2} - \frac{l_1}{2} - R_d\cos\theta\right)\right\}, \quad (3)$$

$$u_d(t) = R_d\omega\left\{\cos\theta + \sin\theta\left[l_3^2 - \left(\frac{L}{2} - \frac{l_4}{2} - R_d\cos\theta\right)^2\right]^{-0.5} \times\left(\frac{L}{2} - \frac{l_4}{2} - R_d\cos\theta\right)\right\}. \quad (4)$$

The configuration of the computational domain is illustrated in Fig. 2. As seen, the domain is axisymmetric, allowing the engine cycle to be simulated by using two-dimensional mathematical model. The engine is very small with a core cylinder radius of just 0.0205 m, thus the flow inside the engine can remain laminar even at relatively high engine speed. In addition, due to its small size, the engine is not equipped with a regenerator, and regeneration is performed by the working gas flowing forwards and backwards between the expansion and compression chambers through the narrow gap formed by the displacer and the inner wall of core cylinder; that is, the solid material of the core cylinder is acting like regenerator material to store and release heat. Such a simple

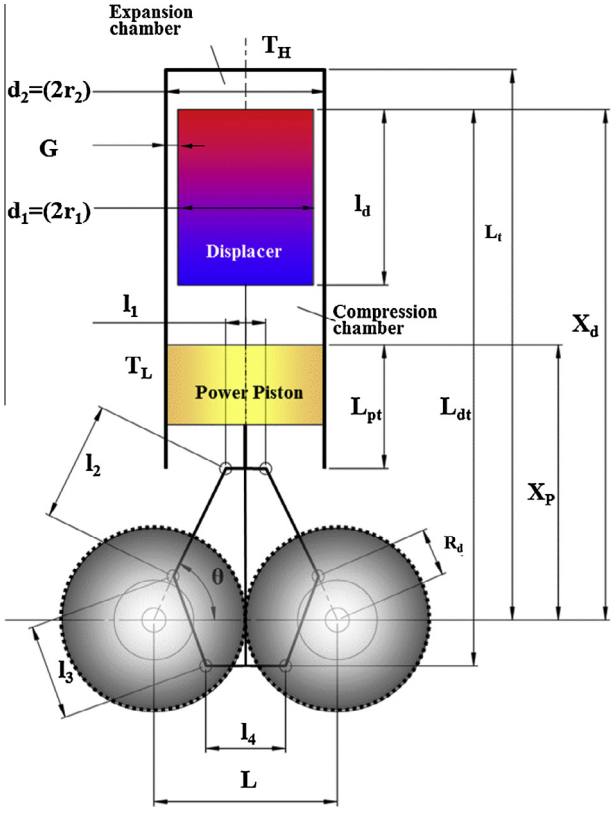

Fig. 1. The configuration and definition of geometric parameters of the β-type Stirling engine.

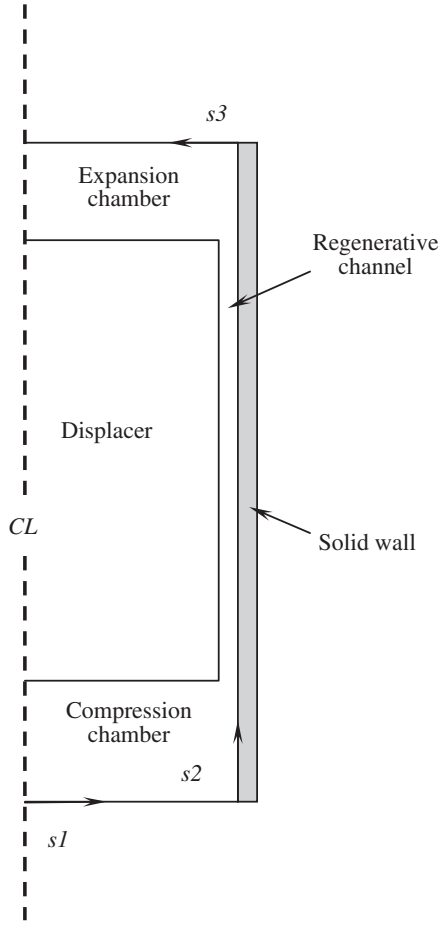

Fig. 2. Schematic of the computational domain.

engine is ideal for the study of basic Stirling engine cycle. The assumptions made to facilitate CFD simulation are as follows: fluid viscosity and thermal properties of all materials are assumed constant, the working gas is air and assumed to be ideal gas, and effects from mechanical friction and thermal radiation are ignored. Therefore, the flow and heat transfer phenomena of the engine cycle can be solved by transient two-dimensional axisymmetric laminar and compressible Navier–Stokes equations plus energy equation and ideal gas equation of state as follows [17]:

Continuity equation:

$$\frac{\partial \rho_f}{\partial t}+\frac{\partial}{\partial x}(\rho_f \tilde{u})+\frac{1}{r}\frac{\partial}{\partial r}(\rho_f r \tilde{v})=0. \tag{5}$$

Momentum equations:

$$\frac{\partial}{\partial t}(\rho_f u)+\frac{\partial}{\partial x}(\rho_f \tilde{u} u)+\frac{1}{r}\frac{\partial}{\partial r}(\rho_f r \tilde{v} u) = \rho g-\frac{\partial p}{\partial x}+\mu\frac{\partial}{\partial x}\left(\frac{\partial u}{\partial x}\right)+\frac{u}{r}\frac{\partial}{\partial r}\left(r\frac{\partial u}{\partial r}\right)+\frac{\mu}{3}\frac{\partial}{\partial x}(\nabla\cdot V), \tag{6}$$

$$\frac{\partial}{\partial t}(\rho_f v)+\frac{\partial}{\partial x}(\rho_f \tilde{u} v)+\frac{1}{r}\frac{\partial}{\partial r}(\rho_f r \tilde{v} v) = -\frac{\partial p}{\partial r}+\mu\frac{\partial}{\partial x}\left(\frac{\partial v}{\partial x}\right)+\frac{u}{r}\frac{\partial}{\partial r}\left(r\frac{\partial v}{\partial r}\right)+\frac{\mu}{3}\frac{\partial}{\partial r}(\nabla\cdot V)-\frac{\mu v}{r^2}. \tag{7}$$

Energy equation:

In gas:

$$\frac{\partial}{\partial t}(\rho_f T_f)+\frac{\partial}{\partial x}(\rho_f \tilde{u} T_f)+\frac{1}{r}\frac{\partial}{\partial r}(\rho_f r \tilde{v} T_f) = -\frac{1}{c_{pf}}\left[\frac{\partial p}{\partial t}+\nabla\cdot(pV)-p(\nabla\cdot V)\right]+\frac{k_f}{c_{pf}}\left[\frac{\partial}{\partial x}\left(\frac{\partial T_f}{\partial x}\right)+\frac{1}{r}\frac{\partial}{\partial r}\left(r\frac{\partial T_f}{\partial r}\right)\right] +\frac{\mu}{c_{pf}}\left\{2\left[\left(\frac{\partial u}{\partial x}\right)^2+\left(\frac{\partial v}{\partial r}\right)^2+\left(\frac{v}{r}\right)^2\right]+\left(\frac{\partial v}{\partial x}+\frac{\partial u}{\partial r}\right)^2-\frac{2}{3}(\nabla\cdot V)^2\right\}. \tag{8}$$

In solid:

$$\frac{\partial}{\partial t}(\rho_s T_s)=\frac{k_s}{c_{ps}}\left[\frac{\partial}{\partial x}\left(\frac{\partial T_s}{\partial x}\right)+\frac{1}{r}\frac{\partial}{\partial r}\left(r\frac{\partial T_s}{\partial r}\right)\right]. \tag{9}$$

Equation of state:

$$p\bar{v}=\bar{R}T_f, \tag{10}$$

where $\tilde{u}=u-u_c$, $\tilde{v}=v-v_c$ are relative velocity components between fluid and local moving frame that moves with u_c and v_c respectively in x and r directions. The last term on the right hand side of Eq. (8) accounts for viscous dissipation effect. As argued in Mahkamov [13], this effect is insignificant compared with other heat transfer effects in Stirling engine, thus it can be neglected. The initial conditions are:

$$\theta=0^\circ,\ u=v=0,\ p=101\ \text{kPa},\ T_f=T_s=T_L. \tag{11}$$

Boundary conditions are:At $x=X_p$:

$$u=u_p,\ v=0,\ T_f=T_L. \tag{12}$$

At $x=L_t$:

$$u=v=0,\ T_f=T_H. \tag{13}$$

The surface of displacer is assumed adiabatic, thus the conditions on displacer surfaces are:

$$u=u_d,\ v=0,\ \frac{\partial T_f}{\partial n}=0, \tag{14}$$

where n is the direction normal to the wall of displacer. On the solid/fluid interface (at $r=r_2$):

$$u=v=0,\ k_f\frac{\partial T_f}{\partial r}=k_s\frac{\partial T_s}{\partial r},\ T_f=T_s. \tag{15}$$

The outer wall of the core cylinder (at $r=r_2+\delta$) is assumed to maintain at a fixed temperature distribution:

$$T_s=T_w(x). \tag{16}$$

3. Numerical Procedure

The numerical procedure in this study is based on an in-house unstructured-mesh, fully collocated, finite-volume code, 'USTREAM' developed by the corresponding author. This is the descendent of the structured-mesh, multi-block code of 'STREAM' [18]. In a Stirling engine, the actions of the displacer and the piston cause expansion and compression of the engine volume, thus a moving mesh technique is needed to simulate such variations in volume. There are two commonly used moving mesh techniques: one is adding or deleting cells to change the volume of the computational domain, and the other is to directly change the geometries of cells to expand or compress their volumes. In this study, the second strategy is adopted. The number of cells in the computational domain is fixed, and the expansion or compression of engine volume is performed by moving the local boundaries of cells to increase or decrease the volumes of the cells, and collectively, they can simulate the expansion or compression of the engine volume just like the action of an accordion. The motion of cell boundary creates local moving frame velocity components $\tilde{u}$ and $\tilde{v}$. However, the component $\tilde{v}$ is zero due to the fact that the motions of displacer and power piston are both along the x-direction (axial direction).

Another important issue is to simulate the compressible flow inside the engine. Since USTREAM is a pressure-based SIMPLE [19] finite volume code, the pressure correction equation has to be modified to account for variable density in compressible flows. The pressure-velocity coupling scheme in Lebon et al. [20] is employed here to perform this task.

4. Results and discussion

The dimensions of the simulated β-type Stirling engine are given in Table 1. The working gas is air with the gas constant of 287 J kg^{-1} K^{-1}, and the core cylinder material is stainless steel with density, thermal conductivity, and specific heat of 7840 kg m^{-3}, 43 W m^{-1} K^{-1}, and 0.45 kJ kg^{-1} K^{-1}, respectively. The initial crank angle and gas pressure are zero degree and 101 kPa, respectively. The external wall temperature distribution defined by Eq. (16) is assumed as:

$$T(x)=\begin{cases}300\ \text{K}, & x\leqslant 0.08\ \text{m}\\ 300\ \text{K}+\frac{x-0.08}{0.158-0.08}\times(800-300\ \text{K}), & x>0.08\ \text{m}\end{cases}. \tag{17}$$

Table 1
The dimensions of the geometrical parameters of the β-type Stirling engine.

r_1 (m)	0.02000
r_2 (m)	0.02050
G (m)	0.00050
l_1 (=l_2 = l_3 = l_4) (m)	0.01800
l_t (m)	0.15800
L (m)	0.04200
L_{pt} (m)	0.05093
L_{dt} (m)	0.16374
l_d (m)	0.07946
R_d (m)	0.00360
δ (m)	0.00100

Before the CFD simulation can be performed, the correctness of the code has to be validated. For this purpose, the engine was run under adiabatic condition at a very low engine speed of 60 rpm. The exact p–V relation in a reversible adiabatic cycle of air is $pV^{1.4} = C$, where C is a constant. Since the current CFD code does not consider mechanical friction or viscous heat dissipation, the adiabatic cycle at low engine speed would be close to an ideal reversible adiabatic cycle. Fig. 3 shows the comparison of adiabatic p–V relations between the exact values and the present CFD results. It can be seen that the simulated p–V relation is almost identical to the exact relation, thus validating the correctness of the code. The next step of the CFD simulation is to determine a proper grid and time step interval to obtain grid and time-step independent solutions. In Cheng's study, their baseline engine operated at an engine speed of 2000 rpm with hot and cold ends temperatures of 800 K and 300 K, respectively. An initial attempt to adopt the operation conditions of the baseline engine to perform the grid and time-step independency test was not successful. The solution converged up to the engine speed of 1860 rpm, and at 2000 rpm, the code diverged at a certain time step. Further investigation revealed that at 1860 rpm, the maximum velocity at the regenerative channel is about 44.0 ms^{-1}, and the Reynolds number, calculated by $Re = \frac{v_{max}G}{\nu}$, is 1833, which is close to upper limit of laminar flow. Therefore, at the engine speed of 2000 rpm, the flow could have become turbulent within a certain period in an engine cycle, and the laminar flow model would fail to converge. For the purpose of grid and time-step independency test, a slightly slower engine speed of 1800 rpm was selected. Three different grids with cell numbers of 6264, 7864, and 9260, respectively were tested by using three different time-step intervals of 8.333×10^{-5} s, 5.555×10^{-5} s, and 4.166×10^{-5} s, which respectively correspond to time-step numbers per cycle of 400, 500, and 800. Fig. 4 shows the grid with 6264 cells. Even though this is the coarsest grid, there are 20 cells allocated within the span of the regenerative channel. Cells are concentrated towards all solid boundaries to resolve the flow and thermal boundary layers. For each simulation, about 10 cycles were needed for the solution to become periodical, and each cycle took about 2–4 h in a PC, depending on grid size and time step number in a cycle. Judging from the values of maximum velocity, heat input, and work output within a cycle, grid and time-step independent solutions can be achieved by the grid with 7864 cells at 500 time steps per cycle,

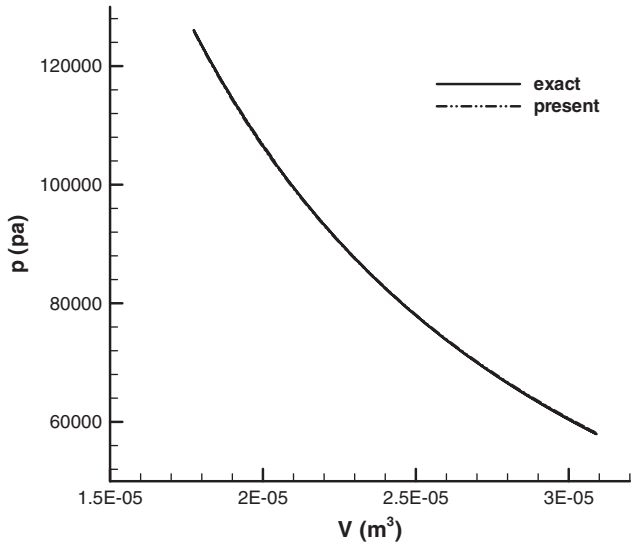

Fig. 3. Comparison of p–V relation between exact values and the present results in an adiabatic cycle with engine speed of 60 rpm.

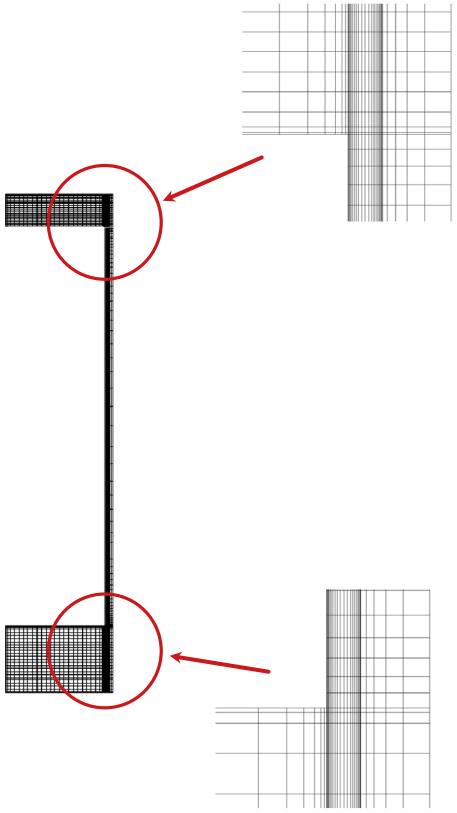

Fig. 4. Computational mesh.

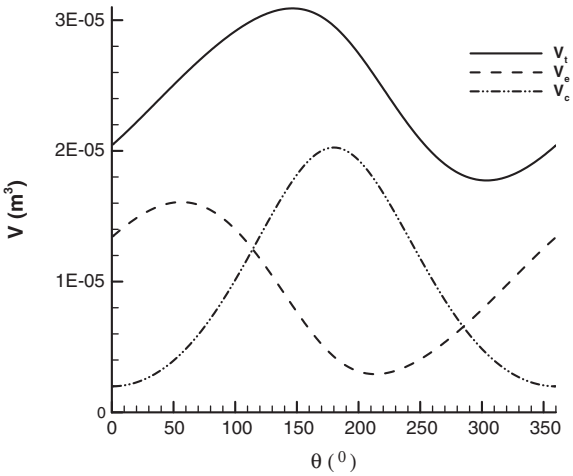

Fig. 5. Variations of total, expansion chamber, compression chamber volumes versus crank angle within an engine cycle.

and this grid and the time step number have been used in this paper. In the following, the discussion will be focused on the case with the engine speed of 1800 rpm.

Fig. 5 shows the variations of total, expansion chamber, and compression chamber volumes versus crank angle over an engine cycle. The maximum and minimum values of the total volume are respectively $3.090 \times 10^{-5}\ m^{-3}$ and $1.774 \times 10^{-5}\ m^{-3}$, giving rise to a compression ratio of 1.742, and they occur at $\theta = 146.16°$ and 303.84°, respectively. It is also noticeable that the maximum volume of the compression chamber is larger than that of the expansion chamber, but the minimum volume of the former is

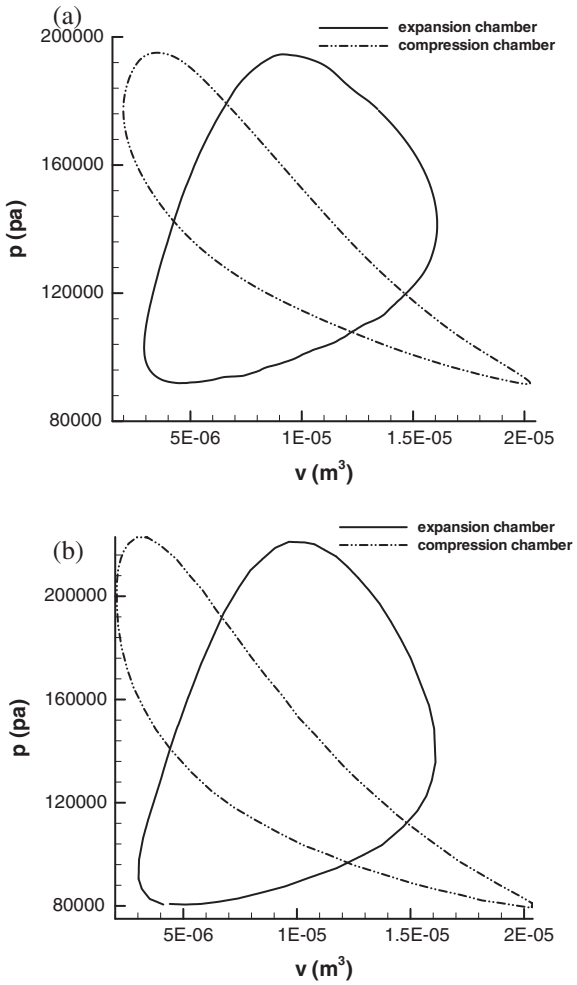

Fig. 6. Variations of averaged pressure versus volume in the expansion and compression chambers (a) current at 1800 rpm, and (b) Cheng and Yu [16] at 2000 rpm.

smaller than that of the latter. That is, the magnitude of volume variation in the compression chamber is larger. The p_{ave}–V diagrams of the expansion and compression chambers are illustrated in Fig. 6(a). Here p_{ave} is the averaged pressure in the individual chamber. Compared with the p–V diagrams in Cheng and Yu [16] (Fig. 6(b)), it has been found that apart from the differences in the magnitudes of minimum and maximum pressure, the tendency of p–V variation in the present study is very similar to that in Cheng's study, which was calculated by an improved variant of the second-order model. This suggests that the simple second-order model is capable of predicting reasonably accurate pressure variations for the current engine. Since the pressure difference caused by gas flow inside the engine is just a tiny fraction of the total magnitude of pressure, the value of pressure is mainly determined by ideal gas equation (Eq. (10)). Therefore, the reason for this similarity should be due to the fact that pressure in the present CFD simulation and in Cheng's second-order model is all obtained by the ideal gas equation.

To demonstrate the general variations of temperature within the engine over an engine cycle, Fig. 7 shows the temperature contours of the entire engine at 10 different crank angles, from $\theta = 36°$ to 360° with an increment of 36°. The motions of displacer and power piston pose different effects on the flow inside the engine. The combined motions of displacer and power piston cause gas to flow forwards and backwards between the expansion and compression chambers, while the motion of the power piston expands or compresses the total volume of the engine, which in turn introduces cooling or heating effects on the working gas. The gas flow that flows forwards and backwards between expansion and compression chambers introduces very strong heat convection effect in both chambers and results in complicated heat transfer behaviors between the gas and the solid boundaries and highly non-uniform temperature distributions across the chambers at any given moment. To this end, it is readily realized that the assumption of uniform temperature distribution and the adoption of constant convective heat transfer coefficients to account for the heat transfer effect in expansion and compression chambers in some second-order models is apparently too crude to represent the real heat transfer behaviors inside the engine. Therefore, the attention is directed towards the investigation on the engine's heat transfer characteristics which can only be analyzed in detail by using CFD approach.

From the expansion and compression chambers' point of view, both go through one phase of receiving gas injection from the other chamber and the other phase of gas ejection to the other chamber through the regenerative channel. These phases are termed "injection phase" and "ejection phase", respectively. Basically, the injection phase of the expansion chamber is the ejection phase of the compression chamber, and vice versa. In the following, the discussion on the flow and heat transfer characteristics is divided into injection phase, ejection phase, and regenerative channel subsections.

4.1. Injection phase

The injection phase in the individual chamber generally coincides with the expansion process of its chamber volume. In the expansion chamber, this is from $\theta = 216°$ to 22° (or 382°); and in the compression chamber, it is from 0° to 198°. As shown in Fig. 7, this phase in the individual chamber can be characterized by the appearance of a major thermal plume in that chamber. However, there is a brief interval, from 0° to 22°, when gas at the lower part of regenerative channel is injected into the compression chamber, and gas at upper part is injected into the expansion chamber. This peculiar phenomenon is due to the downwards motion of displacer that continues to drag gas to the compression chamber and the onset of the expansion process of the expansion chamber that creates vacuum and sucks the gas into expansion chamber. The injection phase poses significant impact on the heat transfer in both chambers. To demonstrate this effect, Fig. 8 shows the enlarged views of velocity vectors and temperature contours as well as local heat flux distributions in the expansion chamber at $\theta = 298.8°$. Fig. 8(a) shows that gas injection produces a plume of cold gas that impinges on the upper heated wall of the chamber (the hot-end wall). This impingement brings the cold gas in direct contact with the hot-end wall, resulting in impingement heat transfer which is well known to be the most effective convective heat transfer mechanism. Therefore, the cold gas get injected into the expansion chamber is rapidly heated up. This can be verified from the distributions of the local heat flux per unit area at $\theta = 298.8°$ along the surfaces of power piston, regenerative channel, and hot end, s_1, s_2, and s_3, given in Fig. 8(b). Here, the surfaces s_1, s_2, and s_3 are defined in Fig. 2, and local heat flux q is calculated by:

$$q = -k_f \frac{\partial T_f}{\partial n}. \tag{18}$$

Under this definition, the heat transfer from solid wall (surrounding) to gas (thermodynamic system) is positive, and that from gas to wall is negative. This particular phase angle was chosen because it corresponds to the maximum local heat flux at the hot-end wall (s_3). Comparing Fig. 8(a) and (b), it can be seen that the

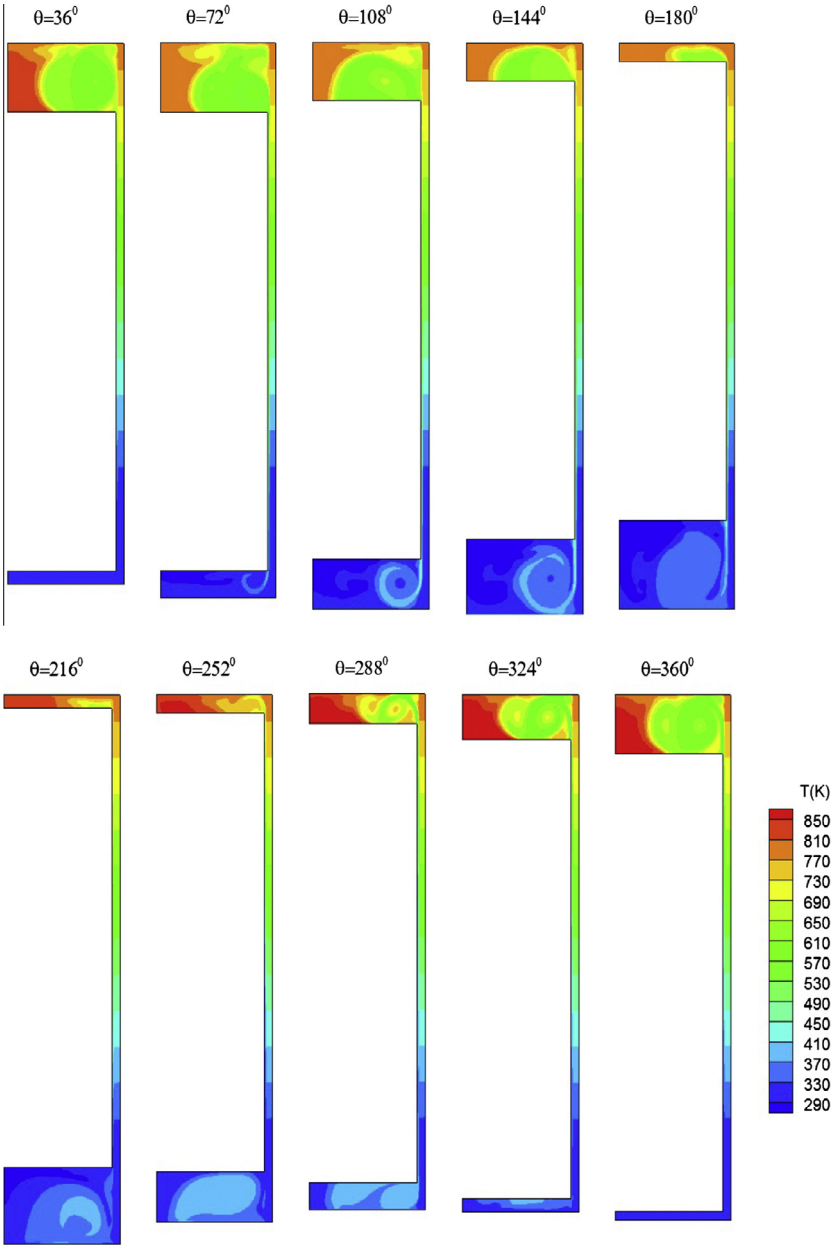

Fig. 7. Temperature contours across the whole engine at 10 different crank angles.

maximum local heat flux (in Fig. 8(b)) occurs within the vicinity of the impingement point (in Fig. 8(a)) of the cold gas jet on the hot-end wall and its value reaches a phenomenal value of 80 kW m^{-2}, which is also the absolute maximum value during the entire engine cycle. As seen in Fig. 8(a), the jet of cold gas forms a primary vortex which in turn induces multiple secondary vortices at its sides. These secondary vortices promote mixing of cold and hot gas and further facilitate convective heat transfer in the expansion chamber. Their effects can be identified by the smaller peaks at both sides of the primary peak on s_3; however, their magnitudes are much smaller than the primary peak produced by the impingement effect. Near the center of expansion chamber, local heat flux is very small as convection becomes very weak. The local heat flux distributions prove that the dominant heat transfer mechanism in the injection phase of the expansion chamber is the impingement of the cold gas on the hot-end wall.

Fig. 9 shows the enlarged views of velocity vectors, temperature contours, and local heat flux distributions of the compression chamber at $\theta = 172.8°$. Similar impingement phenomenon in the expansion chamber can also be observed during the injection phase of the compression chamber, but the impingement results in rapid cooling of the hot gas that enters the compression chamber. The maximum (in terms of absolute value) local heat flux along the cold-end surface s_1 during the injection phase is -24.6 kW m^{-2}. This is much smaller than that in the expansion chamber during its injection phase. In addition, unlike what happened in the expansion chamber, it is neither the maximum local heat flux on s_1 during the entire engine cycle. The real maximum local heat flux on s_1 occurs in the ejection phase which will be discussed in the next subsection.

4.2. Ejection phase

The ejection of gas in expansion or compression chambers is mainly caused by the reduction of volume in the individual chamber. By referring to Fig. 5, this phase is from $\theta = 53°$ to 215° in the

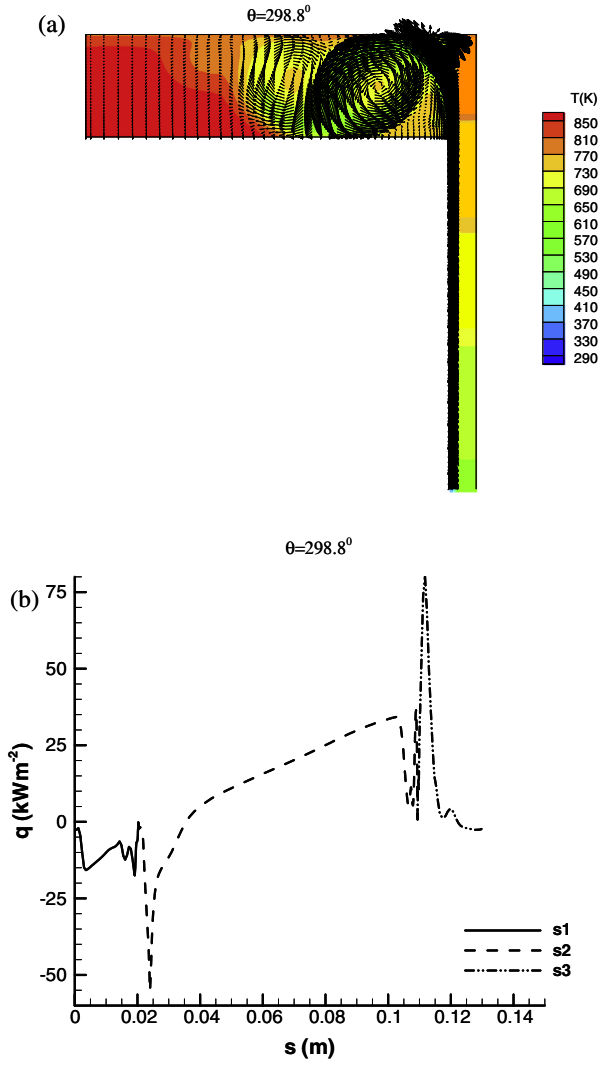

Fig. 8. Temperature contours, velocity vectors, and local heat flux distributions in the expansion chamber at $\theta = 298.8°$; (a) temperature contours and velocity vectors and (b) local heat flux distributions.

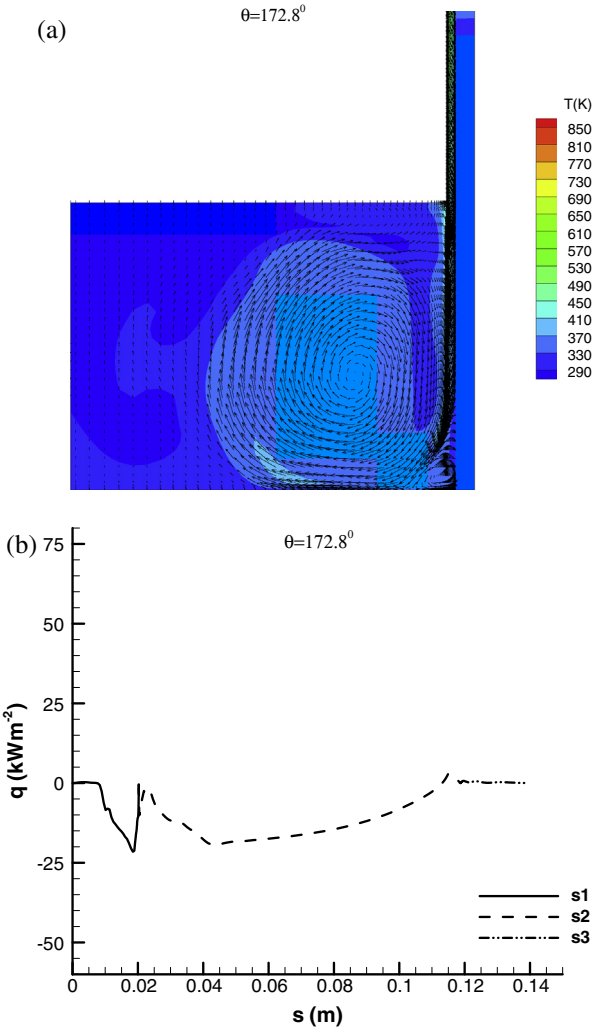

Fig. 9. Temperature contours, velocity vectors, and local heat flux distributions in the compression chamber at $\theta = 172.8°$; (a) temperature contours and velocity vectors and (b) local heat flux distributions.

expansion chamber and from $\theta = 199°$ to $359°$ in the compression chamber. As mention earlier, the reduction of chamber volume is due to the motions of the displacer and power piston. When displacer moves towards the hot end, the volume of expansion chamber is reduced. On the other hand, when displacer and power piston move toward each other, the volume of compression chamber is reduced. In this manner, the displacer and power piston reduce the volume in the individual chamber by decreasing the distance between the upper and lower boundaries of that chamber, and this is equivalent to pushing the gas against the solid walls. In the expansion chamber, the upper wall is the hot end, while in the compression chamber the lower wall is the cold end. The pushing of gas by the displacer and power piston creates an effect similar to impingement that largely compresses the isothermal lines towards the hot or cold ends and increases the local temperature gradient. As a result, it also promotes heat transfer in a way similar to flow impingement does. It can be seen in Fig. 5 that in the compression chamber, the ejection phase mostly coincides with the compression process of the entire engine volume, and the negative heat transfer is further boosted by the compression effect which heats up the gas in the compression chamber and creates even larger temperature difference between the gas and the cold-end wall. The combined heat transfer effects can be demonstrated by velocity vectors, temperature contours, and local heat flux distributions in the compression chamber at $\theta = 230.4°$ shown in Fig. 10. The temperature contours in Fig. 10(a) show that the core temperature in the compression chamber reaches 430 K due the compression process, and the isothermal lines are very dense towards the cold-end wall due to the motion of power piston. Consequently, the local heat flux on s_1 is highly elevated as can be seen in Fig. 10(b). The maximum absolute value reaches 50 kW m^{-2}, which is more than twice the maximum value in the injection phase and is the absolute maximum value on s_1. In the expansion chamber, on the other hand, the ejection phase does not coincide so well with the expansion process of the entire engine volume; therefore, the promotion on positive heat transfer by this mechanism is not very significant. On the contrary, Fig. 5 shows that from $\theta = 150°$ to $220°$, the ejection phase of the expansion chamber coincides with the compression of total engine volume, thus the gas inside the expansion chamber is heated not only by the hot-end wall but also by the compression effect. As a result, the maximum temperature in the expansion chamber reaches as high as 860 K, which is higher than the hot-end temperature. The elevated gas temperature then gives rise to negative heat flux on s_3 as can be seen in Fig. 9(b). This indicates that heat output is not confined to the cold end but can occur at hot end within a short interval during an engine cycle.

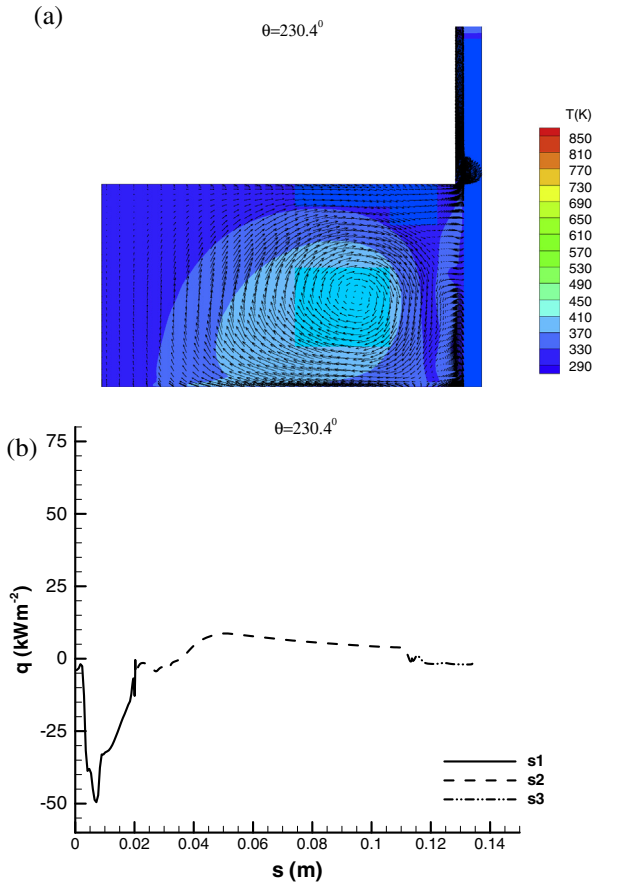

Fig. 10. Temperature contours, velocity vectors, and local heat flux distributions in the compression chamber at $\theta = 230.4°$; (a) temperature contours and velocity vectors and (b) local heat flux distributions.

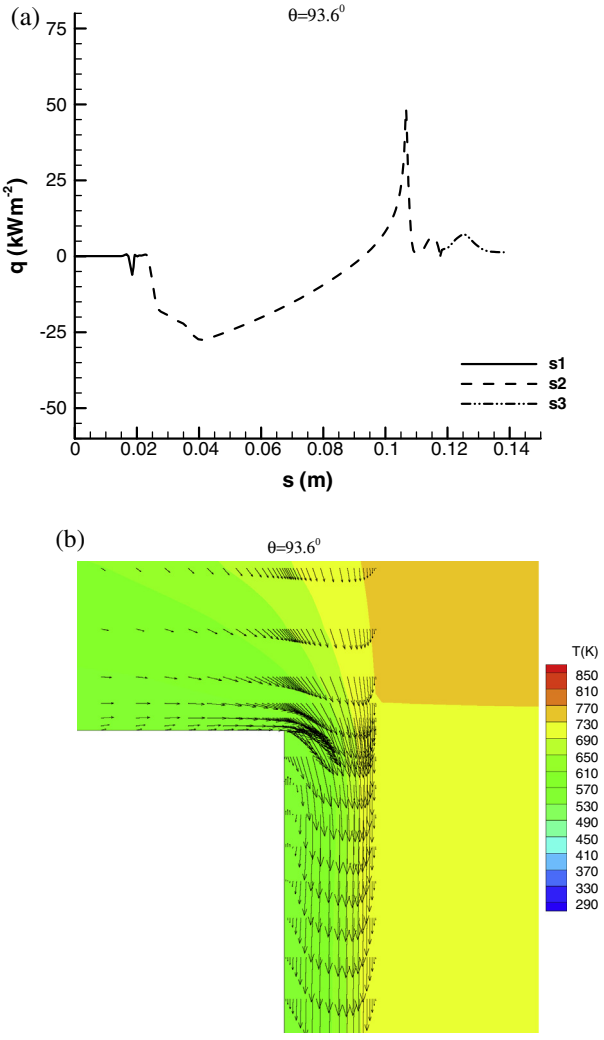

Fig. 11. Temperature contours, velocity vectors, and local heat flux distributions near the entrance of regenerative channel in the expansion chamber at $\theta = 93.6°$; (a) local heat flux distributions and (b) temperature contours and velocity vectors.

4.3. Regenerative channel

The major function of a regenerative channel is to pre-heat the gas during the injection phase of the expansion chamber and to pre-cool the gas during the injection phase of the compression chamber. From the local heat flux distributions shown in Figs. 8(b) and 9(b), it can be seen that the regenerative channel performs this task relatively well as the heat flux on s_2 in Fig. 8(b) is mostly positive (heating gas), and that in Fig. 9(b) is mostly negative (cooling gas). However, there are exceptions. In the ejection phase of the compression chamber, Fig. 8(b) shows that at the lower section of s_2 (near entrance of the regenerative channel), heat flux is negative. This happens when the gas with a temperature higher than the regenerative-channel wall temperature from the compression chamber enters the regenerative channel. The higher gas temperature in the compression chamber is due to the heating of gas by the compression effect mentioned in Section 4.2. Exception also occurs in the ejection phase of the expansion chamber. Fig. 11 shows that distributions of local heat flux and velocity vectors and temperature contours in the vicinity of the entrance of the regenerative channel in the expansion chamber at $\theta = 93.6°$. In Fig. 11(a), a large spike of positive heat flux is visible downstream the entrance region, indicating that gas is heated in this part of regenerative channel. The reason is due to the discharge of some low temperature gas into the regenerative channel as can be seen in Fig. 11(b). The low-temperature gas exists because of the non-uniform heating of gas in the expansion chamber during its injection phase. Although very effective, the impingement heat transfer mentioned in Section 4.1 is also highly concentrated at some localized region. As seen in Fig. 7, this results in a pocket of gas in the expansion chamber that has not been well heated and remains at relatively lower temperature. Fortunately, these exceptions only appear in small localized regions of the regenerative channel and they only last for some brief moments. The regenerative channel actually functions as it is designed to function at the majority of time in an engine cycle. In the following, attention will be focused on discussing average and integrated quantities such as average temperature variation, heat input, and work output within an engine cycle.

4.4. Average and integrated quantities

Since some second-order model adopt a very simple practice to account for heat transfer, it is interesting to see what level of accuracy such practice can achieve. Cheng and Yu [16] has illustrated the distributions of temperature and rates of heat transfer in the expansion and compression chambers. As mentioned earlier, those results are for engine speed of 2000 rpm, which is about 11% higher than the current engine speed of 1800 rpm. However, we can still compare the similarity in the tendency of the variations of some quantities returned by their second-order model and the current CFD approach. The distributions of average temperature and rate

of heat transfer in the expansion and compression chambers by the current study are given in Figs. 12 and 13, respectively. Results from Cheng's study were also digitalized and plotted in these figures for comparison. Note that Cheng used time as the *x*-axis in their plots. Fig. 12 shows that there appears some similarity in the tendency of temperature variations. Yet, there are some major differences. One is the minimum temperature in the expansion chamber happens at different crank angle; and another is that the current study predicts a prolong period of low temperature that results in almost zero heat transfer in the compression chamber, which is not captured in Cheng's results. Fig. 13 shows that the similarity in the tendency of heat-transfer-rate variation is much worse. Fig. 13(a) shows the presence of multi peaks and valleys in the heat-transfer-rate variations in both chambers within an engine cycle. The results from the second order model in Fig. 13(b), on the other hand, only predicts a single peak and a single valley in the expansion chamber and two peaks and two valleys in the compression chamber. The complex variations in heat transfer rate are rooted in the complicated heat transfer mechanisms that result in highly non-uniform temperature distributions mentioned in the earlier sections. Using

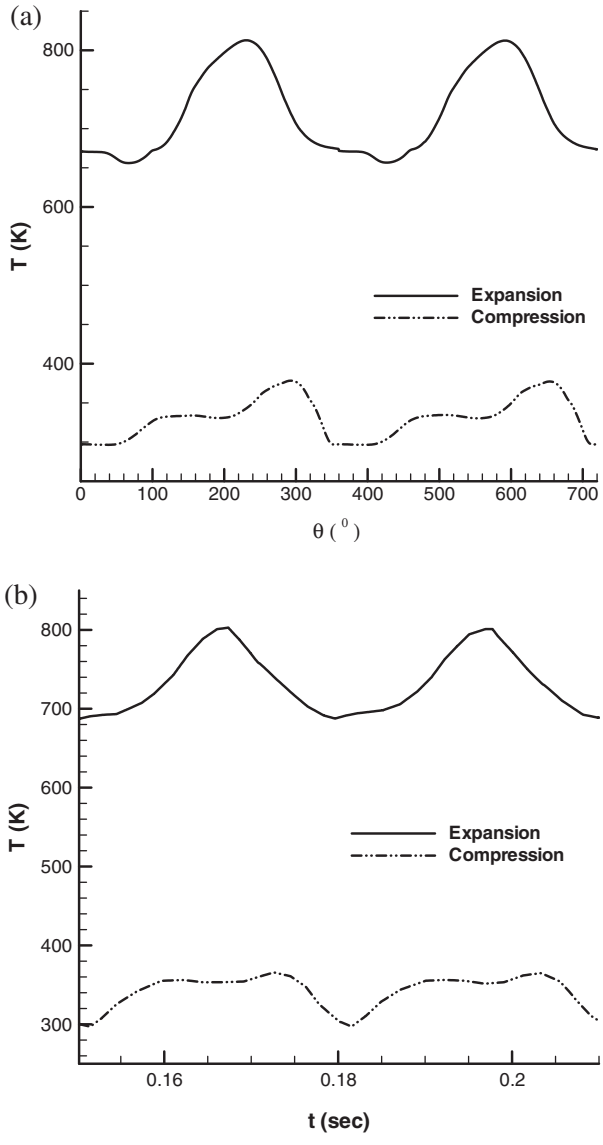

Fig. 12. Variations of average temperature in the expansion and compression chambers; (a) current at 1800 rpm, and (b) Cheng and Yu [16] at 2000 rpm.

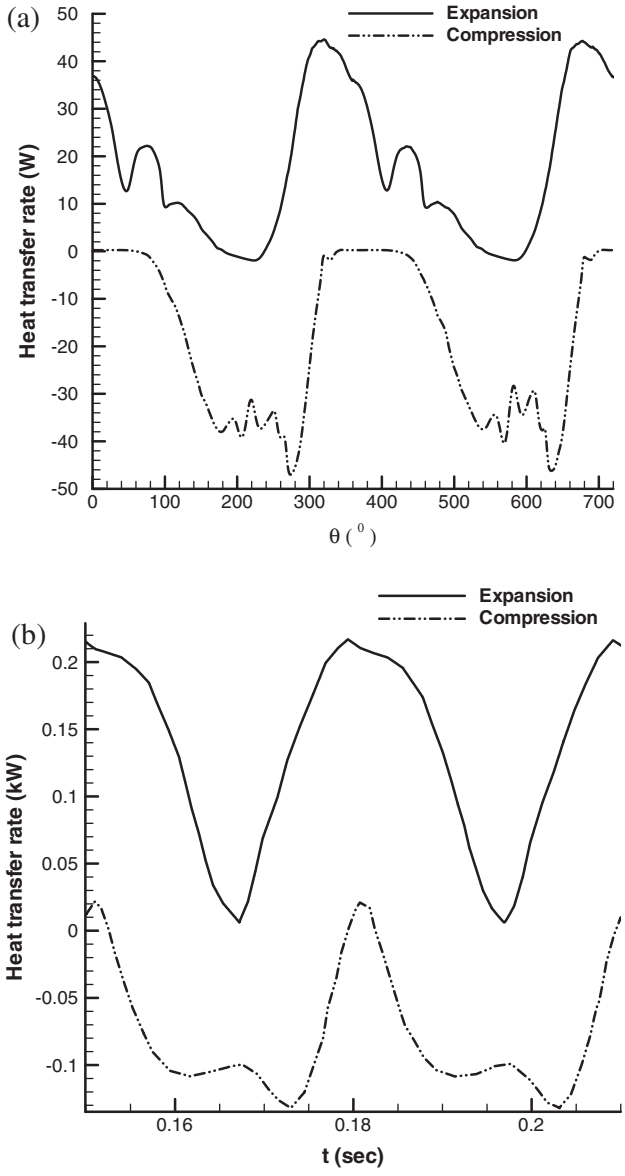

Fig. 13. Variations of heat transfer rates in the expansion and compression chambers; (a) current at 1800 rpm, and (b) Cheng and Yu [16] at 2000 rpm.

the data in Figs. 12 and 13, heat transfer coefficient can be evaluated by:

$$h = \frac{Q}{T_w - T_{ave}}, \tag{19}$$

where T_w is either the hot-end temperature T_H or the low-end temperature T_L respectively at the expansion or compression chamber. The distributions of heat transfer coefficient obtained are illustrated in Fig. 14. As seen, the heat transfer coefficients are not uniform in both chambers, and there are some anomalies of huge oscillations from positive to negative (or negative to positive). The anomalies indicate that simple equation such as (19) would fail to account for the heat transfer effect when applied to the CFD results. To this end, it is clear that the practice of using constant heat transfer coefficient to calculate heat transfer rate in some second-order models fails to account for the effects produced by impingement, mixing of gas, and non-uniform heating, and hence, such a model is not capable of predicting rates of heat transfer very accurately in both chambers.

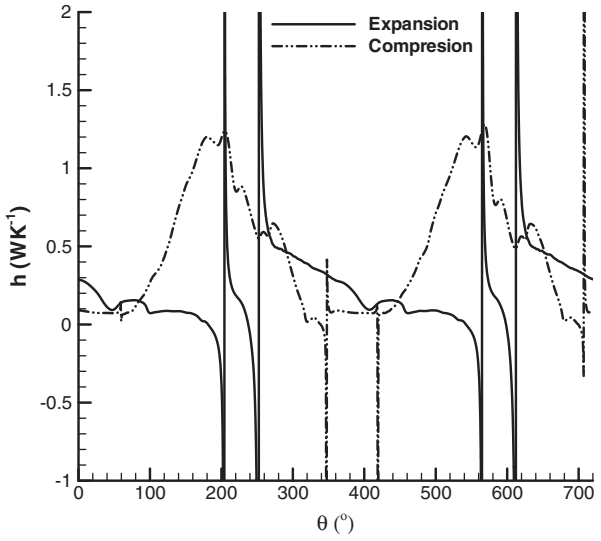

Fig. 14. Distributions of convective heat transfer coefficients calculated by Eq. (19).

From the discussion in the previous subsections, it can be realized that heat input and output can happen at the hot end, cold end, and in the regenerative channel. Therefore, the integration of heat input cannot be confined just along the wall of the expansion chamber. Neither can the integration of heat output be confined along the wall of compression chamber. The rates of heat input and output are calculated by integration along all solid boundaries:

$$Q_{in} = \frac{\omega}{2\pi} \int_{t=t_0}^{t=t_o+t_p} \int_{s=0}^{s=s_1+s_2+s_3} 2q\, dA\, dt, \quad \text{if } q > 0, \tag{20}$$

$$Q_{out} = \frac{\omega}{2\pi} \int_{t=t_0}^{t=t_o+t_p} \int_{s=0}^{s=s_1+s_2+s_3} 2q\, dA\, dt, \quad \text{if } q < 0, \tag{21}$$

where the upper and lower limits in the inner integration mean that the integration is performed along walls of compression chamber, regenerative channel, and expansion chamber. In terms of the evaluation of output power, the focus is on the surface of the power piston because this is the exact place engine work is delivered. The power is calculated by:

$$W = -\frac{\omega}{2\pi} \oint \int_0^{r_2} p 2\pi r\, dr\, dx, \tag{22}$$

where the negative sign on the right hand side of equation is to account for the fact that positive work occurs when dx is negative, and the circular integration is from minimum X_p to maximum X_p and back to minimum X_p. The calculated rates of heat input, heat output, and power are 82.5 W, 69.7 W, and 11.7 W, respectively, resulting in a thermal efficiency η of 14.2%. Here, η is calculated simply by dividing the engine power by the rate of heat input. Ideally, the total heat flow in the regenerative channel should be zero. The heat flow rate along the wall of the regenerative channel in this case is calculated as 1.512 W, which is very small compared with the rates of heat input.

To help readers understand the dynamic processes inside the current Stirling engine, five videos have been made. The files named "temperature", "vector", "flux", "expansion", and "compression" respective play the transient variations of temperature contours, velocity vectors, local heat flux, and enlarged temperature contours and velocity vectors in expansion and compression chambers within an engine cycle.

5. Conclusion remarks

An in-house CFD code has been developed and applied to a rhombic-drive β-type Stirling engine to study the heat transfer characteristics in the thermal cycle of the Stirling engine. The CFD approach allows the heat transfer characteristics to be investigated in great detail. The results include temperature contours, velocity vectors, and distributions of local heat flux at several important time steps in an engine cycle as well as average temperature variations, integrated rates of heat input, heat output, and engine power. Some conclusion remarks from this study can be drawn as follows:

1. The complicated heat transfer behaviors in the engine result in highly non-uniform temperature distributions in all chambers at most of the time in an engine cycle. The assumption of uniform chamber temperatures and the use of constant heat transfer coefficients to account for heat transfer adopted by some zero- or one-dimensional models are too crude to reflect the reality.
2. In the injection phase, impingement heat transfer is the major heat transfer mechanism which allows gas to be heated (in expansion chamber) or cooled (in the compression chamber) very effectively. However, this effect tends to concentrated at some localized region, resulting in non-uniform heating or cooling of gas.
3. In the ejection phase, the motions of displacer and power piston also create a sort of heat transfer effect similar to impingement, but this effect acts on a much larger region and also promotes heat transfer effectively especially in the compression chamber where the negative heat transfer is further boosted by the compression of the entire engine volume.
4. The regenerative channel functions as it was designed for at most of the time within an engine cycle. It pre-heats or pre-cools gas as gas is injected into the expansion or compression chamber. However, exceptions can occur near both regenerative channel entrance regions at some brief moments.
5. Rates of heat transfer in both expansion and compression chambers cannot be predicted very accurately by those second-order models which adopt a very simple practice to account for heat transfer effect.

The future work includes: 1. a parametric study on some important geometrical factors to understand their impact on engine performance and 2. the introduction of a regenerator filled with porous medium into the engine model to more realistically account for the regeneration effect.

Acknowledgments

This work was supported by the National Science Council, Taiwan, Republic of China, under the Grant Number NSC 102-2221-E-168-019 and the Vice-rectory of Research and Industrial Support of the Costa Rica Institute of Technology, Costa Rica, under the Grant Number VIE-5402-1490-1901. The authors are very grateful for their financial support.

Appendix A. Supplementary material

Supplementary data associated with this article can be found, in the online version, at http://dx.doi.org/10.1016/j.enconman.2014.08.040.

References

[1] Tyagi SK, Kaushik SC, Singhal MK. Parametric study of irreversible Stirling and Ericsson cryogenic refrigeration cycles. Energy Convers Manage 2002;43:2297–309.

[2] Formosa F, Despesse G. Analytic model for Stirling cycle machine design. Energy Convers Manage 2010;51:1855–63.

[3] Solmaz H, Karabulut H. Performance comparison of a novel configuration of a beta-type Stirling engines with rhombic drive engine. Energy Convers Manage 2014;78:627–33.

[4] Kazimierski Z, Wojewoda J. Comparison of externally heated air valve engine and the helium Stirling engine. Energy Convers Manage 2014;80:357–62.

[5] Paepe MD, D'Herdt P, Mertens D. Micro-CHP systems for residential applications. Energy Convers Manage 2006;47:3435–46.

[6] Thomas B. Benchmark testing of micro-CHP units. Appl Therm Eng 2008;28:2049–54.

[7] Li T, Tang D, Li Z, Du J, Zhou T, Jia Y. Development and test of a Stirling engine driven by waste gases for the micro-CHP system. Appl Therm Eng 2012;33–34:119–23.

[8] Mahkamov K. An axisymmetric computational fluid dynamics approach to the analysis of the working process of a solar Stirling engine. J Sol Energy Eng 2006;128:45–53.

[9] Parlak N, Wanger A, Elsner M, Soyhan HS. Thermodynamic analysis of a gamma type Stirling engine in non-ideal adiabatic conditions. Renew Energy 2009;34:266–73.

[10] Karabulut H, Aksoy F, Qzturk E. Thermodynamic analysis of a β type Stirling engine with a displacer driving mechanism by means of a lever. Renew Energy 2009;34:202–8.

[11] Timoumi Y, Tlili I, Nasrallah SB. Design and performance optimization of GPU-3 Stirling engines. Energy 2008;33:1100–14.

[12] Abdelsattar H, Gamal M, Talaat W, Abdelnasser M, Leheta M. Computational fluid dynamics – based analysis and optimization of Stirling engines: an insightful survey. In: Proceedings of international conference on energy systems and technologies 2011 (ICEST 2011). p. 29–39.

[13] Mahkamov K. Design improvements to a biomass Stirling engine using mathematical analysis and 3D CFD modeling. J Sol Energy Eng 2006;128:203–15.

[14] Zhigang L, aramura Y, Kato Y, Tang D. Analysis of a high performance model Stirling engine with compact porous-sheets heat exchangers. Energy 2014;64:31–43.

[15] Chen WL, Wong KL, Chang YF. A computational fluid dynamics study on the heat transfer characteristics of the working cycle of a low-temperature-differential γ-type Stirling engine. Int J Heat Mass Transf 2014;75:145–55.

[16] Cheng CH, Yu YJ. Numerical model for predicting thermodynamic cycle and thermal efficiency of a beta-type Stirling engine with rhombic-drive mechanism. Renew Energy 2010;35:2590–601.

[17] Richard HFP. Fluid dynamics. Ohio: Charles E. Merrill; 1973.

[18] Lien FS, Chen WL, Leschziner MA. A multiblock implementation of a non-orthogonal, collocated finite volume algorithm for complex turbulent flows. Int J Numer Method Fluid 1996;23:567–88.

[19] van Doormaal J, Raithby G. Enhancements of the SIMPLE method for predicting incompressible flows. Numer Heat Transf 1984;7:147–63.

[20] Lebon GSB, Patel MK, Djambazov G, Pericleous KA. Mathematical modelling of a compressible oxygen jet entering a hot environment using a pressure-based finite volume code. Comput Fluids 2012;59:91–100.